California Institute of Technology

Ae104c

Measuring Compliant Surface Motion for Fluid-Structure Interaction in Supersonic Flow

Submitted By :
Guillaume Beardsell
Joel Lawson
Mallory Neet

Contents

List of Figures

1 Abstract

Understanding the interactions between supersonic fluids and compliant solid surfaces is of importance for engineering high-speed aircraft. In an effort to advance the fundamental behavior of these fluid-structure interactions, a project is underway in GALCIT to observe a shock impinging on a rectangular compliant panel. This experimental series will be conducted in the Ludwieg tube. A displacement measurement technique needs to be developed and validated that is compatible for use with the Ludwieg tube; this technique must resolve sufficiently high frequencies and be sensitive to the expected amplitudes. This report contributes towards this development process by testing two techniques: single-point measurement via laser displacement sensor (LDS), and full-field measurement via single-camera diffraction-assisted 3D digital image correlation (DAIC). Testing was carried out *ex situ* with a compliant panel being oscillated in a controlled manner. The LDS performed well, being able to resolve frequencies in excess of 1 kHz and amplitudes on the order of 1 μm, and with the correct specification should function well *in situ*. Preliminary results were obtained with DAIC, but improvements to optics and experimental setup are required before quantitative data can be generated; however, the appearance of virtual images during early testing makes this a feasible technique for use within the time and length scales of the proposed experiment.

2 Introduction & Background

2.1 Aerospace Applications

Effective design of air-breathing hypersonic cruise vehicles, such as the Boeing X-51 depicted in Figure 1, need to take into account the strong coupling between the high-speed flow environment and the vehicle. To reduce the vehicle mass and thus improve its efficiency, engineers are likely to consider light-weight, thin structures which are prone to deformations under aero-induced loadings. There is thus a need to characterize the response of such compliant structures to supersonic flows. However, due to the high cost of instrumenting a hypersonic vehicle, there is little experimental data available on the interactions of such a compliant structure with a hypersonic flow [1], thus prompting a need to characterize compliant structures in a laboratory setting.

Figure 1: The Boeing X-51 mounted under the wing of a B-52. Retrieved from [2].

2.2 Caltech Research

Within the hypersonics group at Caltech there is a visiting student, Masato Taguchi, who is looking to study the effects of shock impingement on a compliant surface in the Ludwieg tube. The current configuration makes it possible to view the flow over the compliant surface with Schlieren imaging. In addition, Masato plans to utilize pressure-sensitive paint on the face of the compliant surface that is in contact with the flow, and a measurement technique on the opposite face of the surface to visualize the out-of-plane deformation. This paper focuses on contributing research regarding two techniques that could be utilized for this out-of-plane deformation measurement.

The structure of the compliant surface was designed and will be constructed by Masato. Figure 2 shows the proposed compliant surface, of dimensions 2.2"×4.4" (5.6×11.2 cm) and surrounding structure that will be implemented in the Ludwieg tube. There is a trip device upstream to ensure turbulent flow over the compliant surface, and further upstream (not a part of the shock-tube insert shown) is a wedge to create an oblique shock that will impinge on the surface.

Previous similar experimental work by NASA researchers investigated the response of compliant panels to supersonic, turbulent, attached and separated flow, as well as intermittent and continuous shock impingement [3]. The panels were found to experience significant dynamic response for frequencies below 1000 Hz. Spottswood also performed similar shock-impingement experiments; his data shows panel vibrations on the order of 0.1 mm [1].

The Ludwieg tube has only two windows, parallel to each other on opposite sides of the tube. A window will also be built into the bottom surface of the compliant surface mount, so that both faces of the surface can be viewed. Figures 3 and 4 show the two possible setups within the Ludwieg tube for the compliant surface. The Schlieren imaging cannot be done simultaneously with the pressure sensitive paint or out of plane deformation measurements, but the two latter techniques can be done simultaneously. The Schlieren setup requires the light source to be opposite the high speed camera, thus utilizing both windows in the Ludwieg tube. For the other two measurement methods, the model will first be rotated perpendicular to its Schlieren configuration so that the compliant surface is now parallel to the windows: one face of the surface will be used for the pressure-sensitive paint experiment, and the second face for the out-of-plane deformation. The selection and testing of techniques that are compatible with the physical constraints of the Ludwieg tube setup are the focus of the remainder of this report.

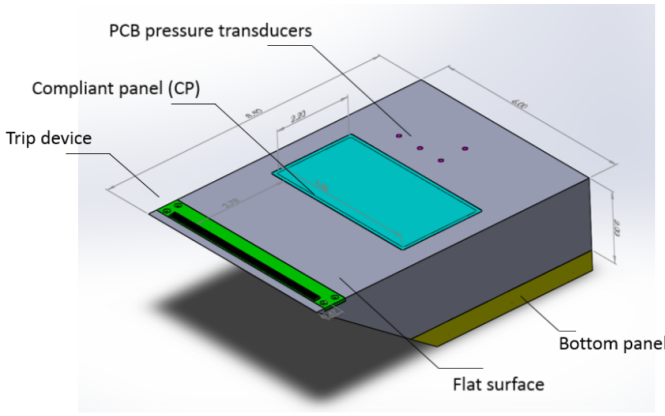

Figure 2: The compliant surface model proposed for use in the Ludwieg tube

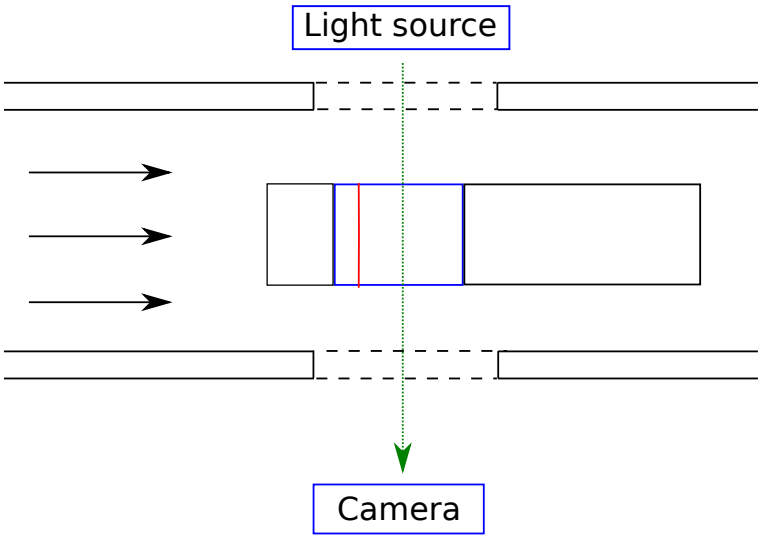

Figure 3: Diagram showing the orientation of the model for Schlieren imaging of the supersonic flow over the model

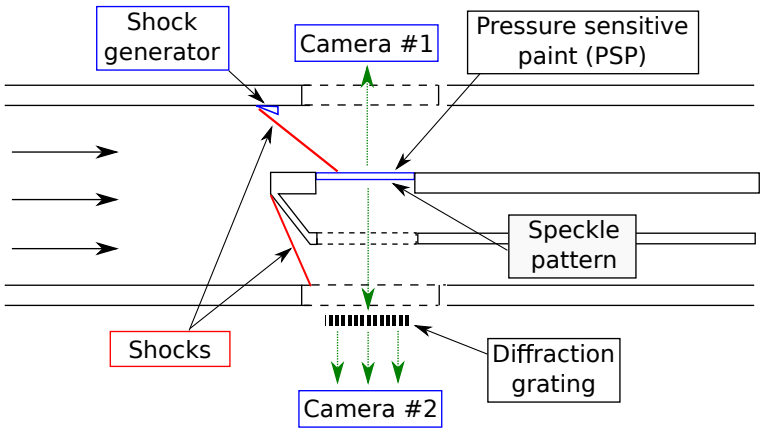

Figure 4: Diagram showing the orientation of the model for simultaneous pressure-sensitive paint/out-of-plane displacement measurements

3 Literature Review

There are a wide range of techniques for measuring the motion of solid surfaces detailed in the literature. At the topmost level, these can be classified either as single-point or full-field techniques. These techniques may measure displacement, velocity or acceleration. Obtaining the time series of one of these allows the other quantities to be deduced via numerical differentiation and integration.

3.1 Single-Point Measurement

Attaching accelerometers to the surface of interest is a simple way of getting single-point motion data. However, this is a contact-based method which may have physical limitations if the surface is undergoing extreme motion or is in a harsh environment. Furthermore, the mass of the accelerometer may not be negligible when used with a thin, compliant panel [4]. There are similar concerns with other contact methods such as strain gages.

Contactless measurements avoid many of these issues. The majority of contactless single-point measurement techniques use a narrow laser beam reflected off a point on the surface. Externally, these techniques all appear very similar, especially since many of them are available as (often literal) 'black-box' commercial devices, and they are often misnamed in advertising literature. However, the underlying principles of operation vary widely, and it is important to understand this since each method has limitations that may lead to erroneous data if applied incorrectly.

3.1.1 Triangulation

A common single-point measurement technique uses laser triangulation. The working principles of this device are depicted in Figure 5.

A laser beam first goes through a focusing lens and is then shone on the (diffuse) compliant surface. Because the surface is diffuse, light is scattered and a portion of it reaches the right-hand side lens. This lens then focuses the light on the CCD detector. Depending on the distance of the panel to the sensor, reflected light will hit a different spot on the CCD detector. Using simple trigonometry, the signal from the CCD detector can then be processed to obtain the displacement of the panel. This processing is usually done internally by the measuring device, which returns a digital signal containing the measured displacement of the plate [5].

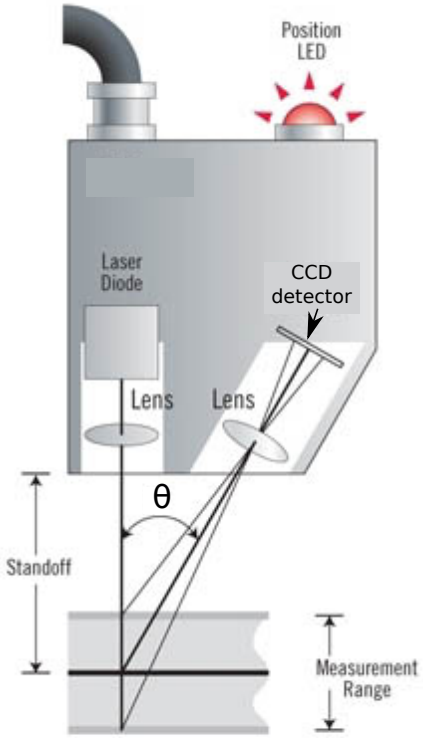

Figure 5: Schematics of a laser triangulation sensor configured for diffuse surfaces. Adapted from [5].

3.1.2 Michelson interferometer

Another single-point measurement device involving a narrow laser beam is the Michelson interferometer, which relies on interference of electromagnetic waves. A monochromatic laser beam first goes through a beam splitter, as depicted in Figure 6. Part of the beam is directed towards a reference mirror, while another part is directed towards the vibrating plate. The reflected beams recombine at the beam splitter and then hit the photodiode. Depending on the path length difference between both beams, the interference will either be positive or destructive, resulting in the photodiode seeing bright or dark fringes respectively. Because the light source is monochromatic, a complete dark-bright cycle corresponds to a displacement

$$d = \lambda/2\,, \tag{1}$$

where λ is the wavelength of the monochromatic light source. One can then infer the magnitude of the orthogonal component of the velocity $|V_\perp|$ of the vibrating plate using

$$|V_\perp| = \frac{\lambda}{2}\Delta t\,, \tag{2}$$

where Δt is the time to complete a full dark-bright cycle.

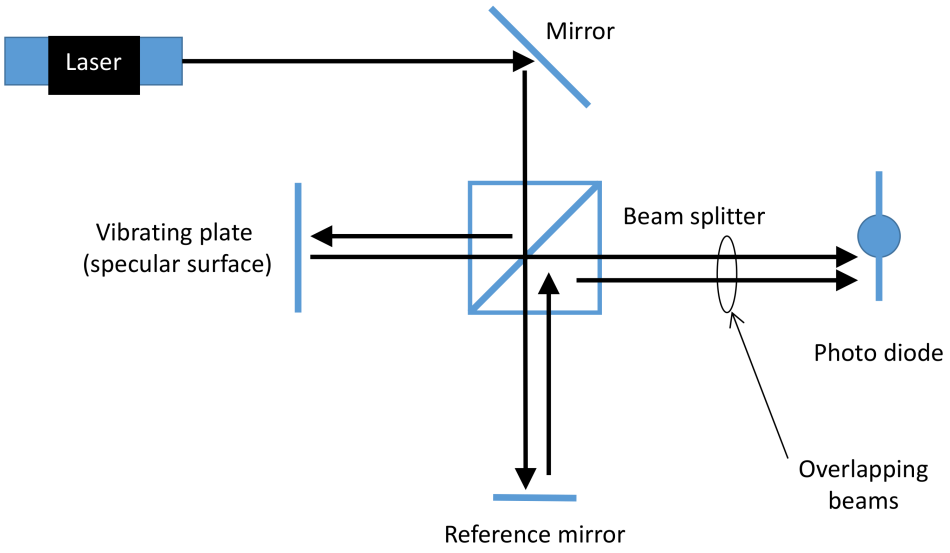

Figure 6: Schematics of the Michelson interferometer.

3.1.3 Laser Doppler vibrometer

One limitation of the Michelson interferometer is that it cannot detect whether the measured object is moving towards the beam splitter or away from it. However, one can use the frequency shift induced by the Doppler effect to infer the direction of the movement. When a monochromatic laser beam with wavelength λ is shone onto a surface moving with velocity V, the reflected beam experiences a frequency shift f_D as a consequence of the Doppler effect:

$$f_D = \frac{2V}{\lambda}\,. \tag{3}$$

To capture the frequency shift of the measurement beam, an acousto-optic modulator (Bragg cell) is inserted in the reference beam, as seen in Figure 7 [6]. This shifts the reference beam by a certain frequency f_B and generates a modulation frequency of the fringe pattern even when the object is at rest. By demodulating the measured signal, one can infer both the magnitude of the velocity $|V_\perp|$ of the vibrating plate and the direction in which it moves, thus recovering the component of the velocity perpendicular to the plate $V_\perp$.

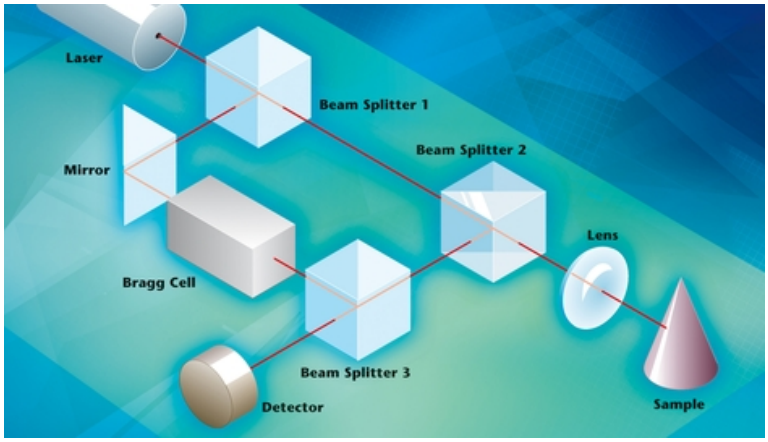

Figure 7: Schematics of a Laser Doppler vibrometer (taken from [6]).

3.2 Full-Field Measurement

Helfrick et al. [7] give an excellent overview of full-field techniques as an introduction to their work with 3D digital image correlation. They note that some common methods are not truly full-field, such as interpolating an array of single-point measurements from multiple accelerometers. Another class are known as 'roving measurements', where a single-point measurement is moved across a surface; an example of this is scanning laser vibrometry. The limitation of such methods is that the surface must remain stationary during the course of a full scan. This makes such techniques unsuitable for measuring dynamic behavior.

3.2.1 Interferometry

Truly full-field measurements often utilize interference effects, which are able to achieve displacement measurements on the order of a wavelength of light [8], e.g. sub-μm in the usual case of visible light. One example of this is holographic interferometry, where a holographic reference image of a surface is recorded using

monochromatic light. Holographs of the displaced surface at a later time are then superimposed with the reference, and the resulting interference pattern can be be used to ascertain the displacement field. For application to this project, holographic interferometry has the advantage of working well at high panel frequencies (> 20 kHz), but it can only give qualitative out-of-plane displacements. Electronic speckle pattern interferometry (ESPI) and digital speckle shearography operate on a similar principle to holographic interferometry: they generate a speckle pattern on the surface by using a highly coherent laser source. This pattern changes as the surface deforms, and a reference pattern is used for interference. These techniques differ mainly in how they generate their reference image; as a consequence, ESPI directly gives displacements whereas shearography gives displacement gradients [9]. However, these techniques also lack truly 3D displacement data.

3.2.2 Digital Image Correlation

Another major class of full-field techniques are digital image correlation methods. Digital images are divided into a grid of 'subsets', and correlation techniques are used to track the motion of these subsets between images in a sequence. Generally, the first image in the series is designated the reference image and all displacements/strains are enumerated with respect to this, but for large displacements one can also specify a dynamic reference where the most recent image in the series is used to correlate with the next image. To assist with correlation, the surface of interest is usually coated with a high-constrast speckle. Typically, this just entails using black and white paint to generate a random pattern of dots. Speckles sized around 5 pixels from the camera's point of view are considered optimal. This can be achieved using off-the-shelf spraypaint, or possibly an airbrush for high-magnification images where smaller speckles are required [10].

2D DIC requires only a single camera, and can be performed adequately using a commerical DSLR camera and in-house or freeware correlation software [11]. However, any out-of-plane motion will be interpreted incorrectly as components of in-plane displacement, so this method is limited to strictly in-plane situations.

Conversely, 3D DIC is able to obtain both in- and out-of-plane displacements by using two cameras that view the surface from different angles. Analysis is more difficult and hence usually needs commercial software, although in-house software has been developed [12]. Further complicating matters is the need to keep the two cameras synced with each other even at high framerates. Such factors mean 3D DIC systems are usually purchased commercially, and these can be prohibitively expensive.

To overcome some of these limitations, multiple research groups have developed DIC methods that can yield 3D data while only using a single camera, thereby reducing the expense and complexity of setup. 3D DIC works by analyzing simultaneous pairs of images from two different perspectives provided by two separate cameras; instead of having two cameras directly obtain these images, various optical techniques can be used to create multiple images of the same surface from different angles. These images can then be focused onto different parts of the sensor of a single camera. The resulting frames can be split to give the required perspectives separately for analysis.

One such method was developed here at Caltech by Xia et al. in Prof. Ravichandran's group [13]–[15]. They refer to their method as diffraction assisted image correlation (DAIC), since it functions by placing a diffraction grating between the surface and the camera. Light rays from the surface that are incident perpendicular to the grating will be transmitted without diffraction (creating an unchanged zeroth-order image), but rays that are incident at some other angle will be diffracted. This will generate additional images symmetrically about the zeroth-order image. DAIC uses only the first-order images either side of the central image. Using ray-tracing, it can be shown that these virtual images appear to originate from a different depth than the actual surface, as illustrated in Figure 8. If in-plane (i.e. 2D) DIC is performed on each of the images to get the in-plane displacement fields, then a simple set of calculations can be used to infer the real out-of-plane displacement field. As a result, 2D DIC software can be used with minimal modification to generate 3D data.

The diffraction grating behavior is governed by Equation (4). For a given slit spacing d and order m, the diffraction angle θ is dependent on the wavelength λ of the incident light. Hence, a surface illuminated by white light will produce a color spectrum of virtual images slightly out of alignment with each other – chromatic aberration. To avoid this and get a well-defined image, Xia uses a monochromatic filter on his light source.

$$d \sin \theta = m\lambda \tag{4}$$

A similar concept was employed by Pankow et al. prior to Xia's work [16]. Here, arrangements of mirrors are used to obtain two angled views of the surface, much like in 'traditional' 3D DIC (see Figure 9). These views are then projected onto a single CCD. This again allows the use of a single camera, thereby reducing expense and the complexity of synchronization. Pankow also mentions the benefit of being able to position the camera further away from potentially damaging tests. One of the validation tests discussed in this paper was actually a high-framerate shock tube

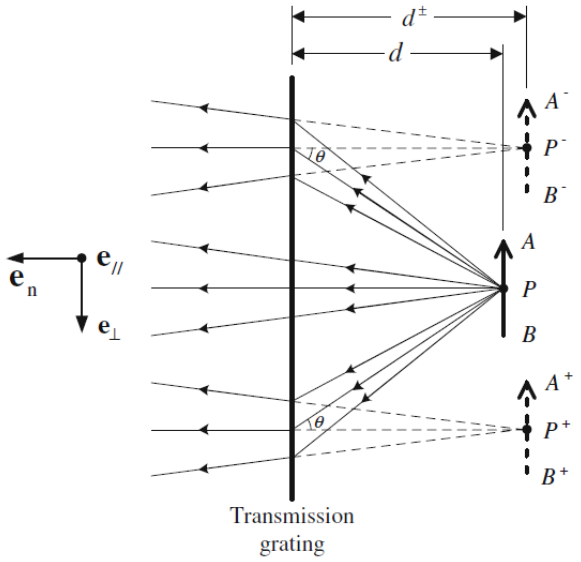

Figure 8: Generation of virtual images from first-order diffraction. Image taken from [13].

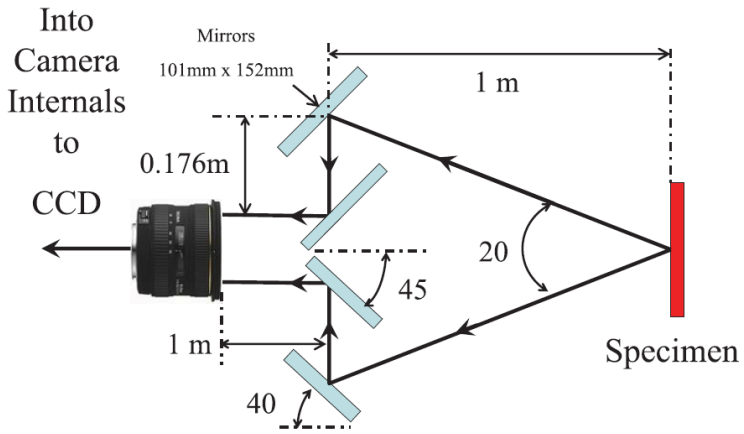

Figure 9: Simulating two-camera DIC using mirrors and a single camera. Image taken from [16].

test. Although an improvement on two-camera 3D DIC, this method still has a more complicated optical path than DAIC, and more importantly, still requires the use of 3D DIC software for analysis since the images are obtained from angled perspectives rather than at right angles.

4 Objectives

- Design a system to measure the out-of-plane displacement of a compliant surface
  - Single point measurements utilizing laser displacement sensor
  - Full field measurements utilizing digital image correlation
  - Implement both measurement techniques on tabletop setup
  - Validate techniques using known frequency inputs
- The measurement techniques chosen should be capable of resolving up to at least 1 kHz vibration modes, and amplitudes below 0.1 mm. These are rough estimates based on prior data from similar work quoted in Section 2.2
- Implement chosen measurement system in Ludwieg tube with existing compliant surface design

5 Experimental Design

In this project, a tabletop setup was used to test the validity of both measurement systems detailed earlier: a laser displacement sensor (LDS) and DAIC, before implementing them in the Ludwieg tube. The goal of this experimental design is to show that both of these techniques can be used to get information about the out-of-plane deformation of the compliant surface in the Ludwieg tube. A list of the materials used in the experiment is given and the specifics of the design follow.

- Steel L-bars
- 1/16" thick polycarbonate sheeting (for compliant surface and diffraction grating mounts)
- 3B Scientific U56001 20 kHz vibration generator
- BK Precision 4011A 5 MHz function generator
- Phantom high-speed camera
- 6"×12" 12,700 and 25,400 lines/inch diffraction gratings (Edmund Optics, stock #54-509 & #40-627)
- LK-G87 laser displacement sensor
- Assorted optical table mounts and hardware
- Narrow-band monochromatic light filter
- NIDAQ and MATLAB data acquisition system
- Black and white matte spray paint

The first step in the experimental design was to make the compliant panel. In this setup the panel is made from an 1/16" thick polycarbonate sheet. This was chosen so that the out-of-plane deformation of the panel would be on the order of mm, any thicker and the sample would not be compliant enough to reach this amplitude. The sheet was cut into two 4"×4" (10.16×10.16 cm) squares. Next, the sample was spray painted with a black matte paint. This was done on both sides of the polycarbonate samples because the LDS used during this experiment, and discussed in more detail later, recommends using a diffuse rather than reflective surface. Finally, one side of each of the polycarbonate samples was speckled using white and black spray paint to create a speckle pattern for the DIC technique. One of the polycarbonate samples is shown in Figure 10.

Next, the stand to hold the polycarbonate sample was made. Figure 11 shows the final structure used to both mount and apply the clamped boundary conditions to

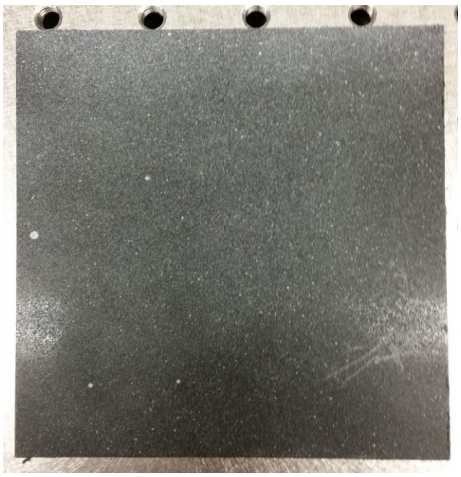

Figure 10: Compliant panel with black-and-white speckle pattern

the compliant surface. In this setup the surface is clamped only along the vertical edges. The structure is made from steel L-bars. L-bars were used to increase the resistance to the bending moment imposed when the surface is perturbed, because we wish to measure only the motion of the plate, with the assumption of rigid surroundings. The plate was mounted so that the exposed dimensions were 10.1 cm $\times$ 6.2 cm. These dimensions are similar to the compliant surface, detailed earlier, that will be put into the Ludwieg tube.

Figure 11: Mounting structure for polycarbonate sample

In order to test the accuracy of the two measurement techniques, a known frequency signal had to be imposed on the plate. This was done by using a vibration generator and signal generator. A second structure was created behind the mounting structure shown in Figure 11 to hold the vibration generator. This secondary structure was created from the same L-bars as the mounting structure. The vibration generator was mounted so that it impacted the plate at roughly the center of the plate from the horizontal and $\frac{3}{4}$ of the way up the plate vertically. For this experiment only the sine wave functionality of the signal generator was used.

The first measurement technique used to measure the out of plane displacement of the polycarbonate plate was a laser displacement sensor. The laser displacement sensor used for the tabletop experiment was the LK-G87 laser displacement sensor manufactured by Keyence. The head of the LDS is depicted in Figure 12. On this figure, (1) points to a glass window through which the laser beam comes out. The reflected light then goes through another glass window (2), behind which the CCD is placed. While in operation, the color of the LED located on the back of the device (6) tells the user whether the sensor is within or outside the measurement range. This allows for an easy calibration of the stand-off distance. Figure 13 shows the dimensions of this particular model, which is designed to have the front face of the sensor 80 mm from the surface. It is capable of measuring displacements of $\pm$15 mm. This is satisfactory for the tabletop validation, but cannot be directly implemented in the Ludwieg tube, as will be discussed in more detail later. The LDS was connected to a NIDAQ data acquisition system and directly linked to MATLAB where the data was collected and then analyzed. The results of these measurements over a range of imposed frequency signals are discussed in Section 6. Figure 14 shows the setup including the laser displacement sensor, which is mounted on a translational stage. This allows the distance of the sensor from the plate to be adjusted easily and accurately. In addition, the vertical location of the LDS can be adjusted. This is useful because the LDS gives only point-wise information about the out-of-plane displacement, thus having the ability to easily measure multiple points gives a greater understanding of the full-field effects.

The second measurement technique used to measure the out-of-plane displacement was the DAIC method detailed previously. First the LDS was removed from the setup discussed above; everything else remained unchanged. Next, the diffraction grating was mounted in front of the plate. For this experiment, plastic film diffraction gratings were used because rigid glass diffraction gratings of this size are both too expensive and take too long to procure for the scope of this project. The gratings were mounted between two 1/16" polycarbonate sheets for rigidity. These sheets introduce additional refraction into the system, however, this will be handled in the DIC code as detailed in Section 7. For this DAIC technique an open source 2D DIC

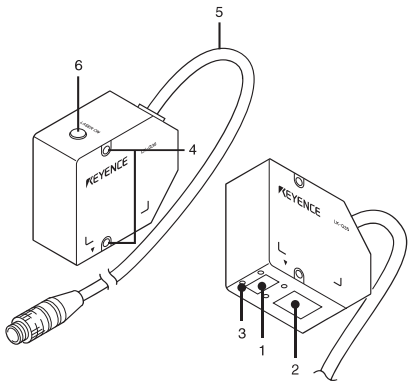

Figure 12: Diffuse LK-G87 module dimensions

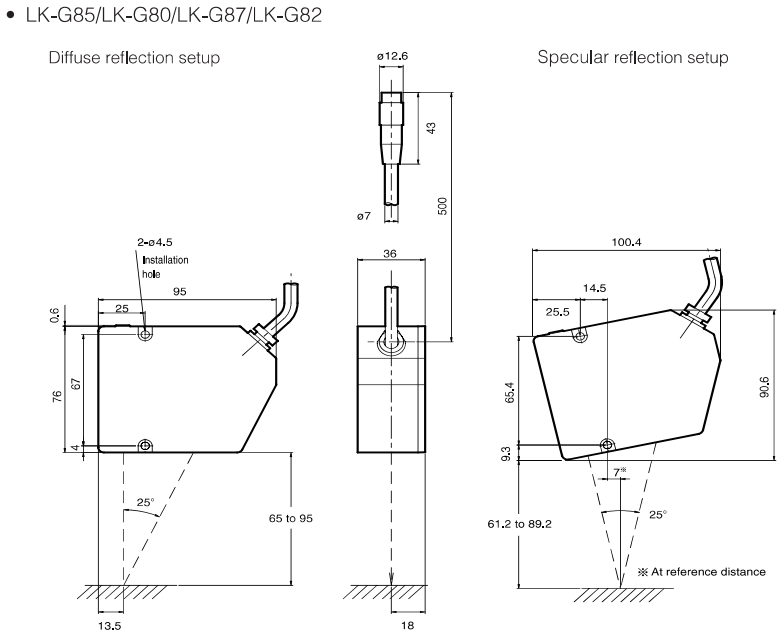

Figure 13: Diffuse versus specular reflection setup for LK-G87 LDS

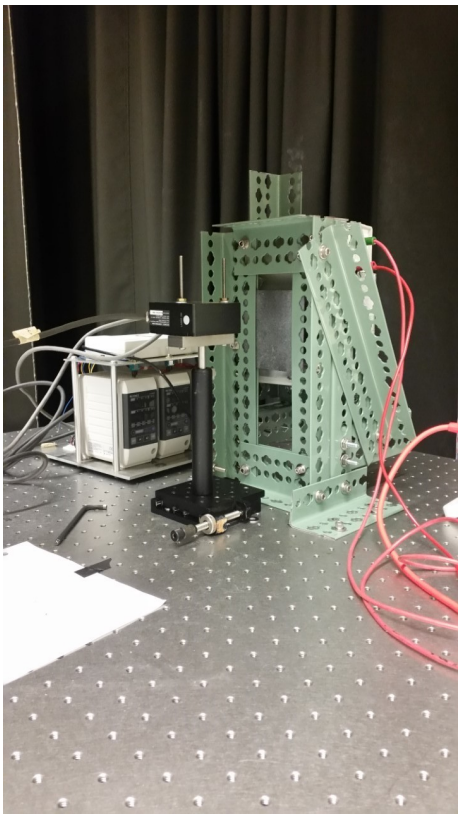

Figure 14: Laser displacement sensor setup

code can be used. Two different diffraction gratings were ordered for this experiment, one with 12,700 lines per inch and one with 25,400 lines per inch. The line spacing dictates how far from the plate the diffraction grating needs to be in order to fit both first-order images into the field of view. For the first diffraction grating listed, the grating is mounted 10.4" from the plate and the second grating is 4.5" from the plate. An example of this diffraction grating setup is shown in Figure 15. Next, the Phantom high-speed camera was placed on the table and focused on the DIC pattern of the plate. The plate was illuminated using a red LED light source in two configurations depending on the distance to the diffraction grating; this was because the light source needed to be positioned such that the light reached the surface of interest without passing through the diffraction grating. Figure 16 shows the full setup for the DIC experiment. The DIC measurement technique was implemented for the same range of frequencies as the laser displacement sensor technique and the results are given in the next section.

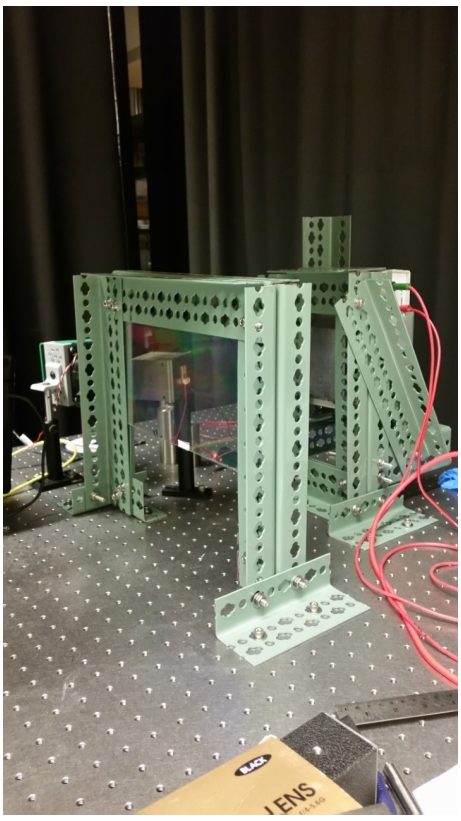

Figure 15: Diffraction grating setup for line spacing of 12,700 lines per inch

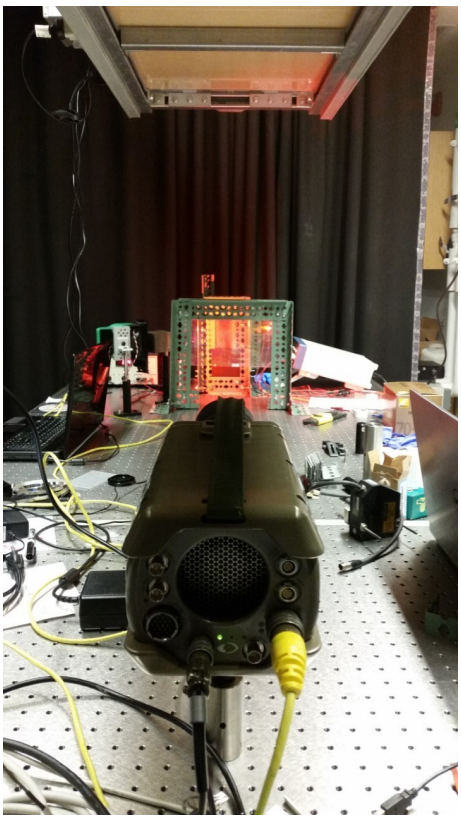

Figure 16: Overall view of the DAIC setup from the camera point-of-view

6 Results

6.1 Laser Displacement Sensor

We obtained steady-state time-series data of the vibrating plate over a range of frequencies between 100 Hz and 1000 Hz. Each data set was obtained at the maximum sampling rate of the LDS (50 kHz) over 1000 periods of the driving frequency. This was to ensure high enough data density to calculate high-resolution frequency spectra. A small time-slice of one of these data sets is shown in Figure 17. At these low amplitudes, the noise is noticeable, yet the underlying sinusoidal function is still clearly visible.

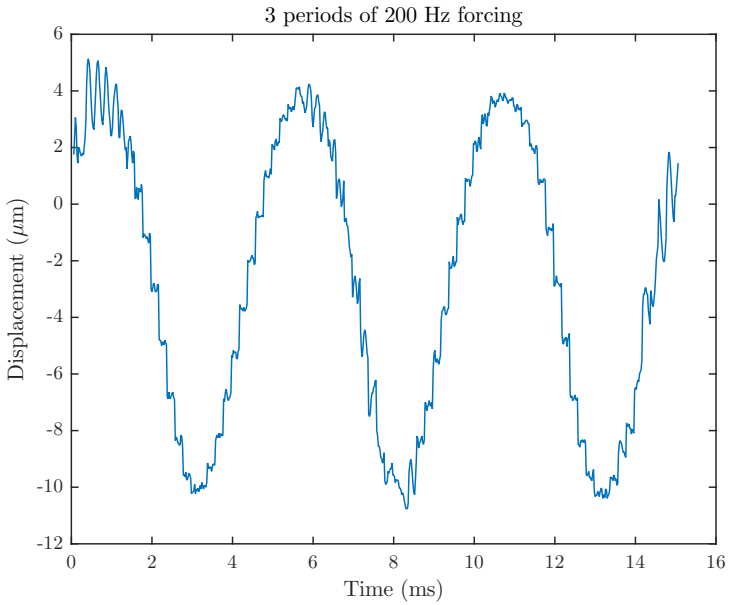

Figure 17: Time-slice of raw data from 200 Hz forcing

We performed frequency analysis on these data. First, a Fourier transform was taken up to Nyquist frequency (25 kHz). These spectra are shown overlaid in Figure 18, where each spectrum has been normalized by its maximum value for ease of comparison, since the lower forcing frequency spectra are otherwise much higher magnitudes than higher forcing frequencies. We observe clear peaks at the forcing frequency for each spectrum except the highest, (1000 Hz), by which point the signal-to-noise ratio is very low. The peak locations were then extracted and plotted against forcing frequency to yield Figure 19. We get a very good match, showing that despite the increasingly poor signal-to-noise ratio as frequency increases, we can still recover the forcing frequency reliably up to 700 Hz.

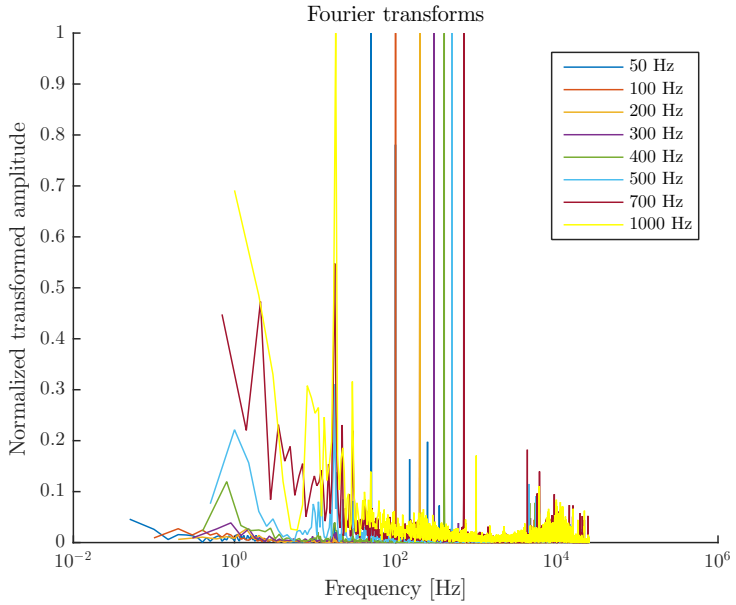

Figure 18: Fourier transforms of the measured response of the panel to different imposed frequencies. In each case, the transform is normalized by the highest amplitude measured.

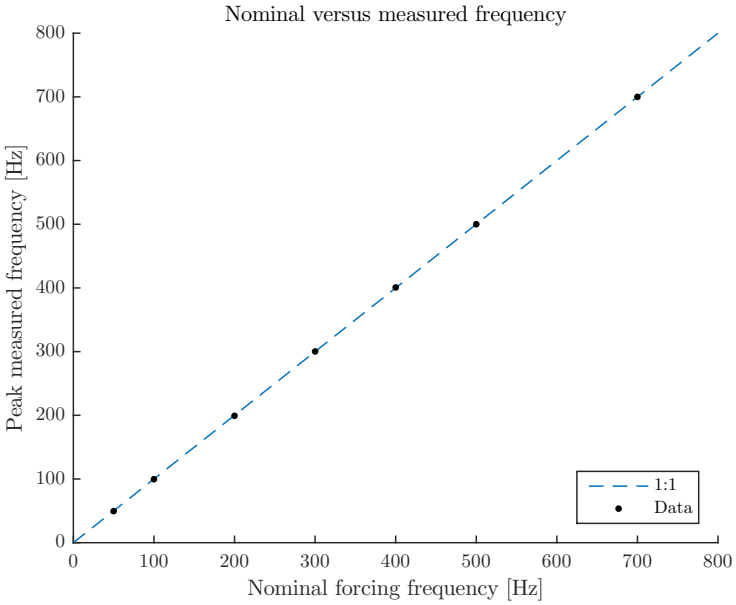

Figure 19: Peak measured frequency as a function of the frequency imposed by the vibration generator.

In Figure 20, the black dots denote the mean amplitude measured for different forcing frequencies. The root mean square (RMS) of the displacement measured by the sensor when the plate is at rest is indicated with a blue dotted line to give an indication of the overall noise level.

It can be seen that as the frequency is increased, the measured amplitude decays. In particular, for $f = 1000$ Hz the measured amplitude is on the order of the noise level. This behavior is due to the vibration generator, which is driven at a constant power.

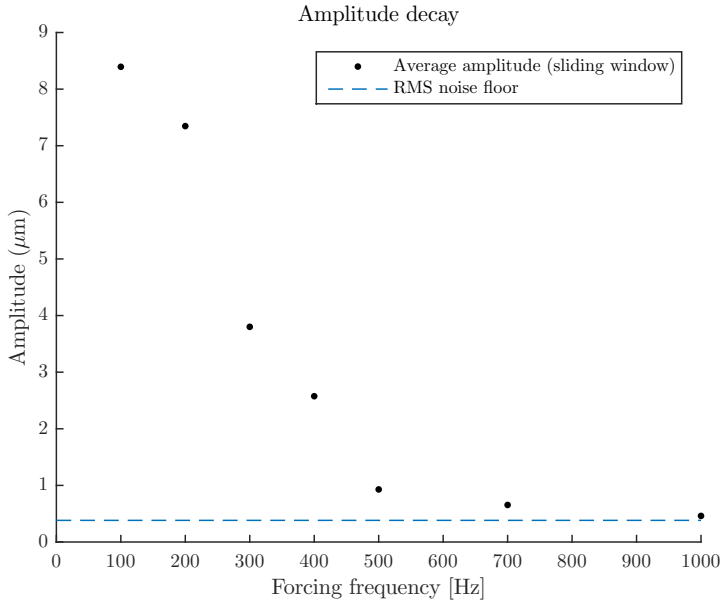

Figure 20: Mean amplitude measured for different forcing frequencies ranging from $f = 50$ Hz to $f = 1000$ Hz. The dotted blue line is the root mean square (RMS) of the displacement measured by the laser triangulation sensor when the plate is at rest.

6.1.1 Noise Analysis

Figure 21 shows the Fourier transform of the displacement measured by the laser triangulation sensor when the plate is at rest, i.e., the combined noise introduced by the environment and the sensor. The maximum amplitude observed is 0.12 μm, close to the repeatability rating of the LK-G 87 (0.2 μm) [17]. Note that the noise maximum amplitude is at $f = 0.12$ Hz whereas we are interested in much higher frequencies ($f \gtrsim 50$ Hz).

In Figures 22a and 22b, we show the Fourier transform of the panel response for

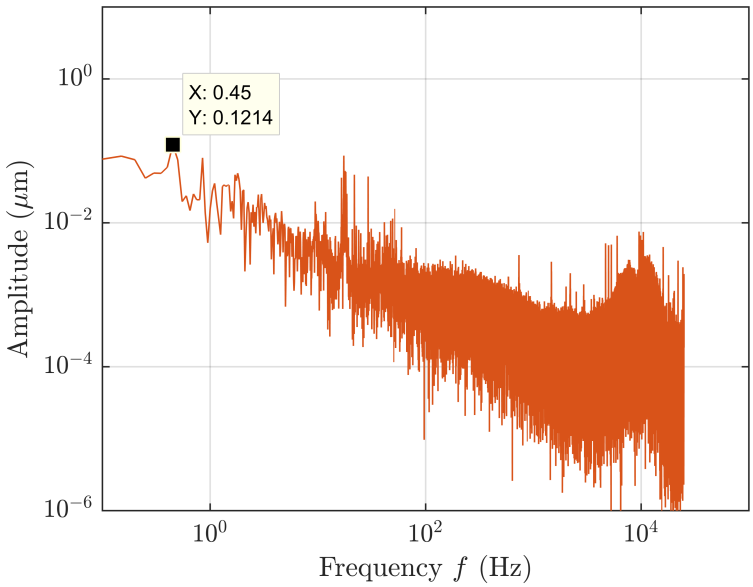

Figure 21: Fourier transform of the displacement measured by the laser triangulation sensor when the plate is at rest.

forced frequencies $f = 200$ Hz and $f = 700$ Hz. It can be seen that in both cases the amplitude of the dominant frequency is above the maximum frequency observed in Figure 21. By comparing the very high frequency content ($f \sim 10^4$ Hz) of Figures 21 and 22, one can see that when the plate is vibrating the very high-frequency content is very different from the resting plate. A possible explanation for this observation is proposed in Section 7.

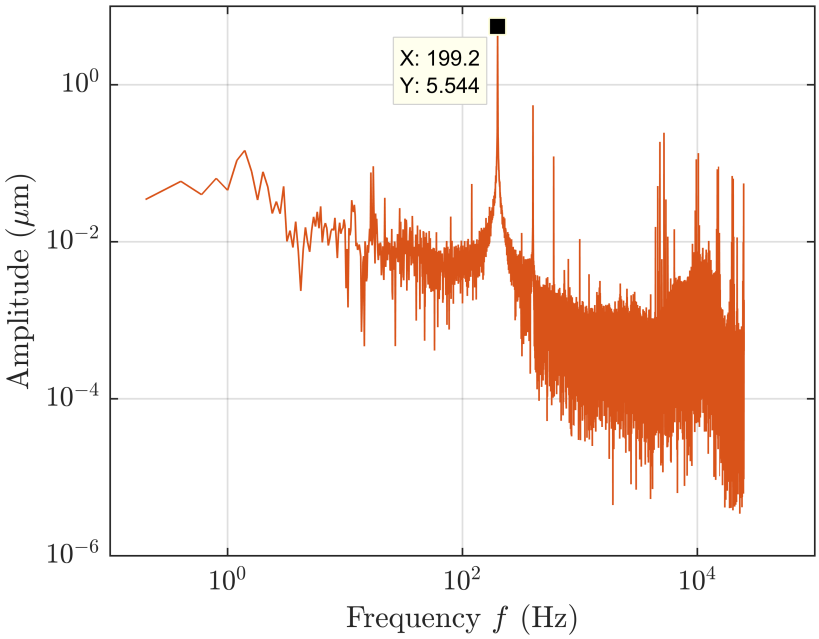

(a) 200 Hz forcing frequency.

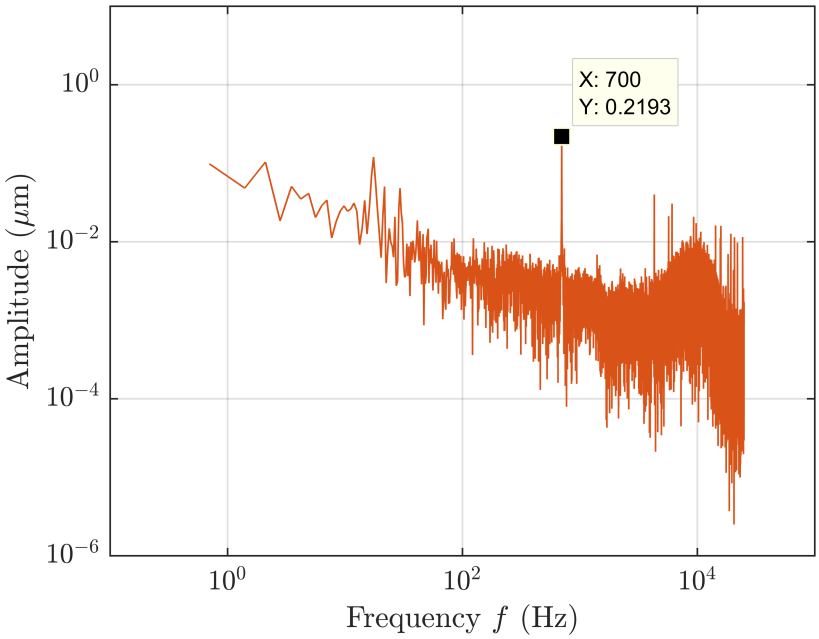

(b) 700 Hz forcing frequency.

Figure 22: Fourier transform of the displacement measured by the laser triangulation sensor for two different forcing frequencies.

6.2 Diffraction-Assisted Image Correlation

Due to time constraints, we were only able to get DAIC partially functional. We had been concerned that the light source would not be bright enough, or that the use of inexpensive film diffraction gratings would not give adequate conditions to view recognizable first-order images. However, we were able to view these images, both via the camera and even with the naked eye. An example of this is illustrated in Figure 23.

Figure 23: Unprocessed still image captured by Phantom camera of a hand and one of the first-order virtual images

Using the approximate wavelength of red light from the LED and the known line spacing of the diffraction gratings, we found the theoretical offset required for the gratings from the surface, as detailed in Section 5 previously. These calculations worked, and we were able to observe first-order diffraction images of the panel entirely contained within the field of view. Unfortunately, the virtual images of the panel were not easily visible due to their low brightness. This is further discussed, along with possible solutions, in Section 7. To be able to visualize these images, we attached a piece of paper with text to the panel, so that there would be a bright square with high-contrast markings. With this addition, we were able to see the virtual images, albeit still out-of-focus and low brightness (Figure 24). To address the brightness issue, ImageJ was used to enhance the concentration locally to one of the virtual images (Figure 25). Somewhat surprisingly given possible deviations

from flatness in our diffraction grating, the virtual images were not heavily distorted from the original, and the text was still reasonably legible.

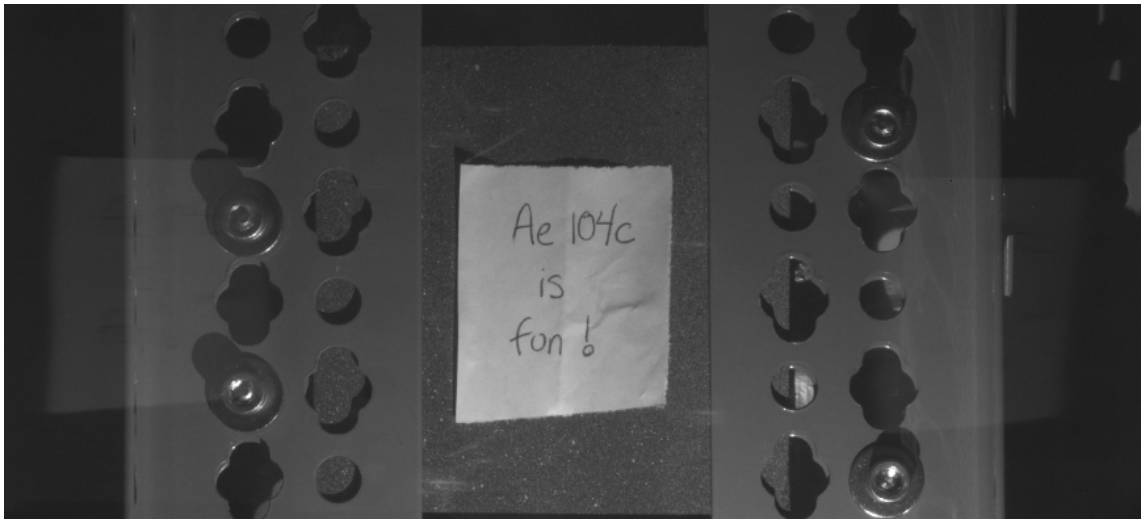

Figure 24: Unprocessed still image captured by Phantom camera of a piece of paper affixed to the panel

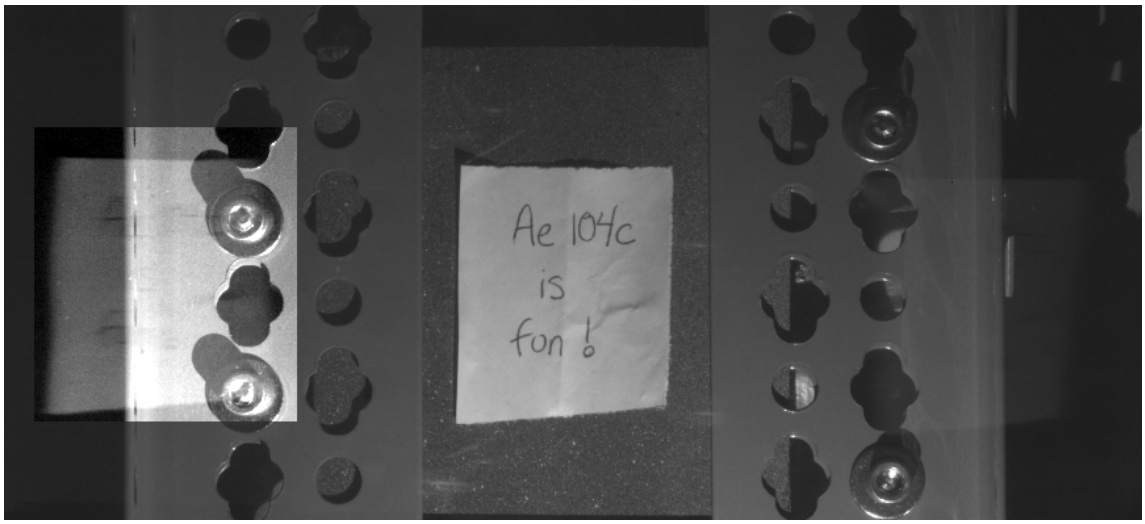

Figure 25: Locally contrast-enhanced version of Figure 24

7 Conclusions & Future Work

Generally, positive results were obtained with the laser displacement sensor. We were able to detect displacements on the order of μm before the signal decayed to the level of the noise. We were also able to detect sinusoidal driving frequencies up to 1 kHz, and in fact this value was not due to limitations in the LDS itself but rather the amplitude of the vibration generator. According to the Nyquist criterion and the listed specifications of the LDS, this value should be able to be considerably exceeded if necessary. Thus we easily met both our frequency and amplitude targets using a single-point measurement technique.

There were some concerns with the data obtained from the LDS. One was the non-white nature of the noise as further detailed in Section 6.1.1. A possible solution to this is to employ a high-pass filter software-side since the highest amplitudes were found at lower frequencies. A second concern was the apparent discretization of the data. This is clearly seen when the raw time-series data is plotted using points rather than just connected by a line: an example is shown in Figure 26.

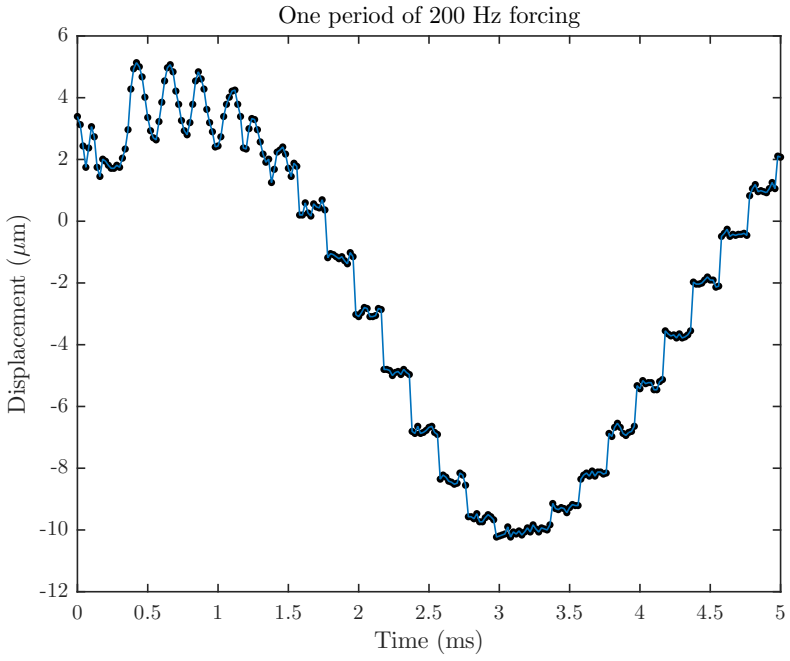

Figure 26: A single period of the time series at 200 Hz forcing, showing individual raw data points

We are not entirely sure what causes this behavior, although our tentative hypothesis hinges on the discrete nature of the CCD sensor internal to the LDS. Figure 27

shows how the laser displacement sensor measures the displacement of the surface. The laser beam leaves the sensor and is initially perpendicular to the surface. The surface then reflects the beam back into the laser displacement sensor to a CCD sensor. As the plate moves the laser beam is reflected back to different CCD pixels. However, the sensor only records a change in position for the surface when the laser beam changes pixels, that is, when the reflected beam moves from one pixel to the next. This effect appears in the plots as small jumps in the data because the sensor measures no displacement and then a sudden change in displacement when the beam is reflected to a different pixel.

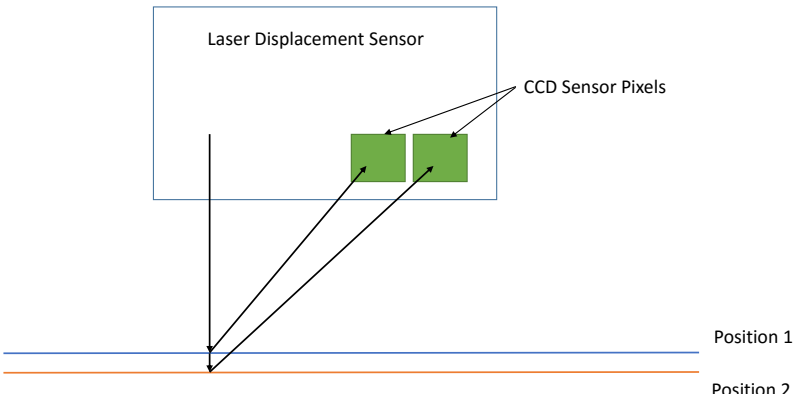

Figure 27: Simplistic discretization mechanism

However, this mechanism does not explain why we see much smaller oscillations within each of these 'levels', as is evident when we zoom in closer on the data. If it were a single bright point traversing a pixel, we would expect uniform amplitude until it crossed to the next pixel. We must remember that the actual operation of the device is more complex. It functions using diffuse, not specular, reflection, and so the laser light is scattered in many directions and the CCD actually observes a speckle pattern [18]. Discretization of the sensor is still likely to be the cause of this phenomenon, but a more detailed study of the inner mechanics of the LDS is required.

There is still much work to be done developing the DAIC method. Additionally, more work needs to be done to incorporate the laser displacement single-point measurement system into the Ludwieg tube. The LDS model used in the table-top setup has an offset of 80 mm. For application in the Ludwieg tube the laser displacement sensor needs to have a range of at least 17" (432 mm). This is the distance from the outer face of the Ludwieg tube window to the approximate centerline of the tube where the sample would be mounted. Keyence has two models in the LK-G series

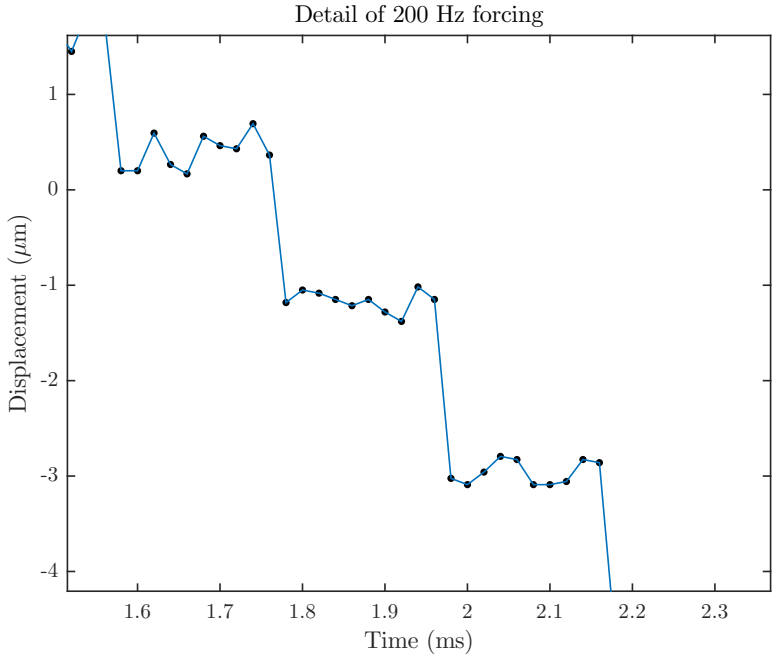

Figure 28: Detail of Figure 26

with ranges of 500 mm: LK-G505 and LK-G507. Either of these models should work with the Ludwieg tube results and provide similar data to the tabletop experiment.

For the DAIC experimental setup the virtual images were difficult to see because the mounting frame for the plate was shiny and the DAIC pattern on the polycarbonate plate is largely matte black, thus the bright image of the frame overlaps and obscures the virtual image of the plate. For future tests this effect can be remedied by painting the frame matte black as well, and additionally, subtraction of a reference image may be able to recover the moving DIC speckle pattern. We also observe that the virtual images are poorly focused. This is possibly due to them being outside the focal plane of the lens used. If this is the case, then selecting a lens with a broader depth-of-field may allow for both the original and virtual images to be captured simultaneously with sufficient focus.

The lighting of the polycarbonate plate for the DIC experiment could also be changed to produce better results. In the current experiment, the plate was illuminated by a red LED from either the side or from the bottom due to the physical limitation of the setup. This caused uneven lighting on the plate and thus uneven brightness in the shadow images. For future experiments the lighting should be integrated into the mount holding the plate. Multiple LED lights mounted around the frame could create a more even brightness over the plate. This will likely eliminate any issues

that could arise in post-processing due to the change in brightness over the surface.

The next big step in the DIC experiment is to implement an open-source 2D DIC code to analyze the images and extract the full-field out-of-plane displacements. One issue that is likely to occur is the refraction added into the system by the two polycarbonate sheets used to hold the diffraction gratings and by the multiple windows of the Ludwieg tube setup. This effect can be added into the code with a simple calculation using Snell's law, $n_2/n_1 = \sin(\theta_1)/\sin(\theta_2)$. The refractive index of polycarbonate is $n = 1.60$. Given that the light is initially propagating through air with a refractive index $n = 1$, then the light is turned toward the normal. The light then travels through the polycarbonate sheet and exits into the air where it is turned back away from the normal. However, the light is now traveling on a line parallel to but offset from the initial path. This effect is shown in Figure 29, and introduces an error into the out-of-plane displacement analysis. However, as stated before, a correction for this should be implementable in the 2D DIC code.

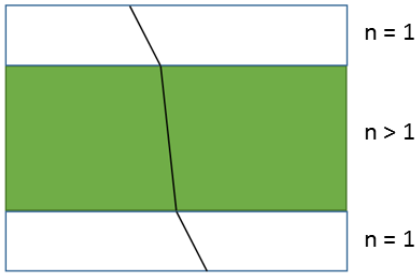

Figure 29: Refraction effect due to Snell's Law

In conclusion, both techniques trialled in this report produced promising results, and we are confident that with sufficient refinement, they can be used to extract useful data as part of the broader experimental campaign. The single-point measurement technique is significantly easier to use and is at a more advanced stage of readiness, by virtue of being a commercial 'black-box' design, although as discussed it is still important to have a good understanding of its mode of operation to avoid unnoticed errors. Preferably, we will be able to use DAIC so that full-field data can be obtained, but LDS is a valuable back-up, and in any case will prove useful in helping to validate data returned from DAIC.

8 Acknowledgements

The authors would like to thank the following people for their contributions and advice towards this project:

- Prof. Austin: initial direction and setting the scope of the project
- Matt Leibowitz: going out of his way to get things sorted for us
- Masato Taguchi: assistance with setup and operation of Phantom camera
- Maria Sakovsky: assistance with setup and operation of laser displacement sensor
- Mike Mello: lots of practical advice on which displacement techniques to pursue and where to find good literature
- Owen Kingstedt: advice on interferometry setup
- Christian Kettenbeil: advice on how to implement DAIC, and offer of help with data processing (although we didn't get that far)
- Andrew Knisely: providing us with a light source
- Denise Ruiz: helping with orders and tracking down our missing diffraction gratings

References

[1] S. Spottswood, T. Eason, and T. Beberniss, "Influence of shock-boundary layer interactions on the dynamic response of a flexible panel", *Proceedings of the ISMA-2012*, pp. 17–19, 2012.

[2] W. Hennigan, *Test flight of aircraft designed to reach mach 6 fails*. [Online]. Available: `http://articles.latimes.com/2012/aug/16/business/la-fi-0816-hypersonic-test-20120816`.

[3] C. Coe and W. Chyu, "Pressure-fluctuation inputs and response of panels underlying attached and separated supersonic turbulent boundary layers", 1972.

[4] N. H. Baharin and R. A. Rahman, "Effect of accelerometer mass on thin plate vibration", *Jurnal Mekanikal*, no. 29, pp. 100–111, 2009.

[5] M. instruments, *Laser triangulation sensors*. [Online]. Available: `http://www.mtiinstruments.com/technology/triangulation.aspx`.

[6] Polytec, *Basic principles of vibrometry*. [Online]. Available: `http://www.polytec.com/us/solutions/vibration-measurement/basic-principles-of-vibrometry/`.

[7] M. N. Helfrick, C. Niezrecki, P. Avitabile, and T. Schmidt, "3D digital image correlation methods for full-field vibration measurement", *Mechanical Systems and Signal Processing*, vol. 25, no. 3, pp. 917–927, 2011.

[8] Rice University, *Physics 332 holographic interferometry*, 2003.

[9] L. X. Yang and Y. Y. Hung, "Digital shearography for nondestructive evaluation and application in automotive and aerospace industries", Rochester, MI.

[10] A. J. Comer, K. B. Katnam, W. F. Stanley, and T. M. Young, "Characterising the behaviour of composite single lap bonded joints using digital image correlation", *International Journal of Adhesion and Adhesives*, vol. 40, pp. 215–223, 2013, ISSN: 0143-7496.

[11] J. M. Lawson, "Damage detection and characterisation in advanced composite aircraft", B.Eng.(Hons), University of Auckland, 2013.

[12] R. M. Stubbing, "DTA digital image correlation capability", New Zealand Defence Technology Agency, Tech. Rep. 1690, 2016.

[13] S. Xia, A. Gdoutou, and G. Ravichandran, "Diffraction assisted image correlation : a novel method for measuring three-dimensional deformation using two-dimensional digital image correlation", *Experimental Mechanics*, vol. 53, pp. 755–765, 2013.

[14] Z. Pan, S. Xia, A. Gdoutou, and G. Ravichandran, "Diffraction-assisted image correlation for three-dimensional surface profiling", pp. 155–165, 2015.

[15] J. Notbohm, A. Rosakis, S. Kumagai, S. Xia, and G. Ravichandran, "Three-dimensional displacement and shape measurement with a diffraction-assisted grid method", pp. 399–400, 2013.
[16] M. Pankow, B. Justusson, and A. M. Waas, "Three-dimensional digital image correlation technique using single high-speed camera for measuring large out-of-plane displacements at high framing rates", 2010.
[17] Keyence, *LK-G series: user's manual*.
[18] R. G. Dorsch, G. Husler, and J. M. Herrmann, "Laser triangulation: Fundamental uncertainty in distance measurement", *Applied Optics*, vol. 33, no. 7, pp. 1306–1314, 1994.

A Appendix

```
clear; clc; close all;
latex_pls
freq = [50 100 200 300 400 500 700 1000];
Fs = 50000; % sampling frequency

% Import into data structure: 'all'
for i = 1:length(freq)
    load([num2str(freq(i))]);
    all.(['f',num2str(freq(i))]).w = data;
    all.(['f',num2str(freq(i))]).t = time;
end
load Noise_only;
noise.w = data;
noise.t = time;
clear data time

% Plot amplitude versus nominal frequency
for i = 2:length(freq)
    amp(i-1) = amp_calc(all.(['f',num2str(freq(i))]).t,...
        all.(['f',num2str(freq(i))]).w,freq(i),Fs);
end
noise_amp = rms(noise.w-mean(noise.w));
figure(1)
hold on
plot(freq(2:end),1000*amp,'k.','MarkerSize',10);
plot([0 1000],1000*noise_amp*[1 1],'--')
hold off
xlabel('Forcing frequency [Hz]')
ylabel('Amplitude ($\mu$m)')
title('Amplitude decay')
legend('Average amplitude (sliding window)','RMS noise floor')
xlim([0 1000])

figure(2)
hold on
for i = 1:length(freq)
    y = all.(['f',num2str(freq(i))]).w;
    evenL = 2*round(length(y)/2); % make sure length is even
    Y_fft = abs(fft(y)); % only keep magnitude
    Y_fft = Y_fft(1:evenL/2); % up to half sampling freq
    Y_fft = Y_fft/max(Y_fft(2:end)); % normalize heights
    F = Fs*(0:evenL/2-1)/length(y); % prepare frequency abscissa
%     if i ~= length(freq)
%         plot(F,Y_fft)
%     end
     plot(F,Y_fft)
```

```
    index(i) = find(Y_fft(2:end) == 1);
    Fmax(i) = F(index(i)+1);
end
set(gca,'xscale','log');
xlabel('Frequency [Hz]')
ylabel('Normalized transformed amplitude')
title('Fourier transforms')
legend_entries = strcat(arrayfun(@num2str, freq,...
    'UniformOutput', false),{' Hz'});
legend(legend_entries)
saveas(gcf,'FFT.pdf')
hold off

figure(3)
hold on
plot([0 800],[0 800],'--')
plot(freq(1:end-1),Fmax(1:end-1),'k.','MarkerSize',10)
xlabel('Nominal forcing frequency [Hz]')
ylabel('Peak measured frequency [Hz]')
title('Nominal versus measured frequency')
legend('1:1','Data','Location','SouthEast')
hold off
```

Listing 1: Main script for analysis of LDS data

```
function [amp] = amp_calc(time,data,freq,sampling_freq)

signalT = 1/freq; % signal period
samplingT = 1/sampling_freq; % sampling period

width = round(signalT/samplingT); % number of indices for a single
    sample period
number_of_windows = floor(length(time)/width);

for i = 1:number_of_windows
    window = ((i-1)*width+1):i*width;
    local_amp(i) = ((max(data(window)))-(min(data(window))))/2;
end

amp = mean(local_amp);

return
```

Listing 2: Function to perform mean amplitude calculation